PCCP

PAPER

View Article Online
View Journal | View Issue

Cite this: *Phys. Chem. Chem. Phys.*, 2015, **17**, 18944

Molecular dynamics of NH_3 induced by core-electron excitation

Noelle Walsh,*[a] Anna Sankari,[a] Joakim Laksman,[b] Tomas Andersson,[a] Shabnam Oghbaie,[a] Feras Afaneh,[c] Erik P. Månsson,[a] Mathieu Gisselbrecht[a] and Stacey L. Sorensen[a]

Received 22nd May 2015,
Accepted 23rd June 2015

DOI: 10.1039/c5cp02959g

www.rsc.org/pccp

Nuclear motion in the $N1s^{-1}4a_1^1$ core-excited state of ammonia is investigated by studying the angular anisotropy of fragments produced in the decay of the highly excited molecule and compared with predictions from *ab initio* calculations. Two different fragmentation channels (H^+/NH_2^+ and $H^+/NH^+/H$) reveal complex nuclear dynamics as the excitation photon energy is tuned through the $4a_1$ resonance. The well-defined angular anisotropy of the fragments produced in the dissociation of the molecular dication species suggests a very rapid nuclear motion and the time scale of the nuclear dynamics is limited to the low fs timescale.

1 Introduction

Core-excited states in molecules are typically very short lived and their spectroscopies can be sensitive to the geometry of the molecule in those states.[1,2] Nuclear motion in the core-excited state prior to electronic decay has been verified for a number of molecules[1–7] and has been observed to influence both electronic decay and fragmentation dynamics (and kinematics).[1,3,8–10]

Reported rapid geometry changes following core-electron excitation[4–6] include the observation of a strong bending motion in H_2O that results in bond rearrangement,[10] an out-of-plane nuclear motion in BF_3[11] and the induction of an umbrella-like bending motion in CH_3.[7] In the case of core-excitation to a potential-energy surface (PES) with repulsive character, an ultrafast bond elongation on the fs-timescale may be initiated within the core-hole lifetime such that dissociation competes with Auger decay. Ultra-fast dissociation[12] in the core-excited state has been documented for a number of molecules.[3,9,13–20]

In this work we investigate the response of NH_3 to core electron excitation to the $4a_1$ molecular orbital. In particular we aim to investigate any nuclear dynamics induced in the molecule as a result of this excitation and how the molecular geometry evolves as the photon energy is detuned through the $N1s^{-1}4a_1^1$ resonance.

To date very different nuclear dynamics have been reported for NH_3 in the $N1s^{-1}4a_1^1$ state. The work of Hjelte[9] provided spectroscopic evidence for ultra-fast dissociation on a timescale comparable to the core-excited state lifetime (~6 fs) – providing confirmation that a rapid extension of an N–H bond along one coordinate of the $4a_1$ PES can take place. In that work, approximately ~1% of cases involved dissociation before Auger decay in the molecule.[9] Meanwhile, Senba[21] and coworkers concluded that a symmetric stretching mode, ν_1, and a symmetric bending mode, ν_2, with periods on the same order of magnitude as the lifetime of the core-excited state are activated upon excitation of an N1s electron to the $4a_1$ orbital. Their data also indicated that the population of stable NH_3^{2+} states as a result of Auger decay from the $N1s^{-1}4a_1^1$ state was influenced by the vibrational state of the core-excited molecule. The present study allows us to gain a better insight into the interplay between these bending and stretching motions.

While electron and fluorescence spectrometries can provide evidence for nuclear motion, the detailed description of the geometric evolution of the molecule is difficult to extract directly from spectroscopic measurements. However, over the last two decades the coincidence momentum imaging technique has been developed and application of this enables the elucidation of molecular geometry.[5,22–25]

Our three-dimensional multi-coincidence ion imaging spectrometer allows us to study the energy sharing between fragments and to determine the angular anisotropy of the fragments produced *via* dissociation following photoexcitation. The setup has been used to shed light on ultrafast nuclear motion in C_2H_2,[6] OCS,[26] CO_2[27] and H_2O.[10] Here, we employ the imaging technique for the study of NH_3.

In its ground state NH_3 has a trigonal pyramidal geometry and belongs to the C_{3v} symmetry group with a H–N–H bond angle of 107.8°.[28] The electronic configuration of this state is

[a] *Division of Synchrotron Radiation Research, Department of Physics, Lund University, Box 118, 22100 Lund, Sweden. E-mail: noelle.walsh@sljus.lu.se*
[b] *MAX IV Laboratory, Lund University, Lund, Sweden*
[c] *Physics Department, The Hashemite University, P.O. Box 150459, Zarqa 13115, Jordan*

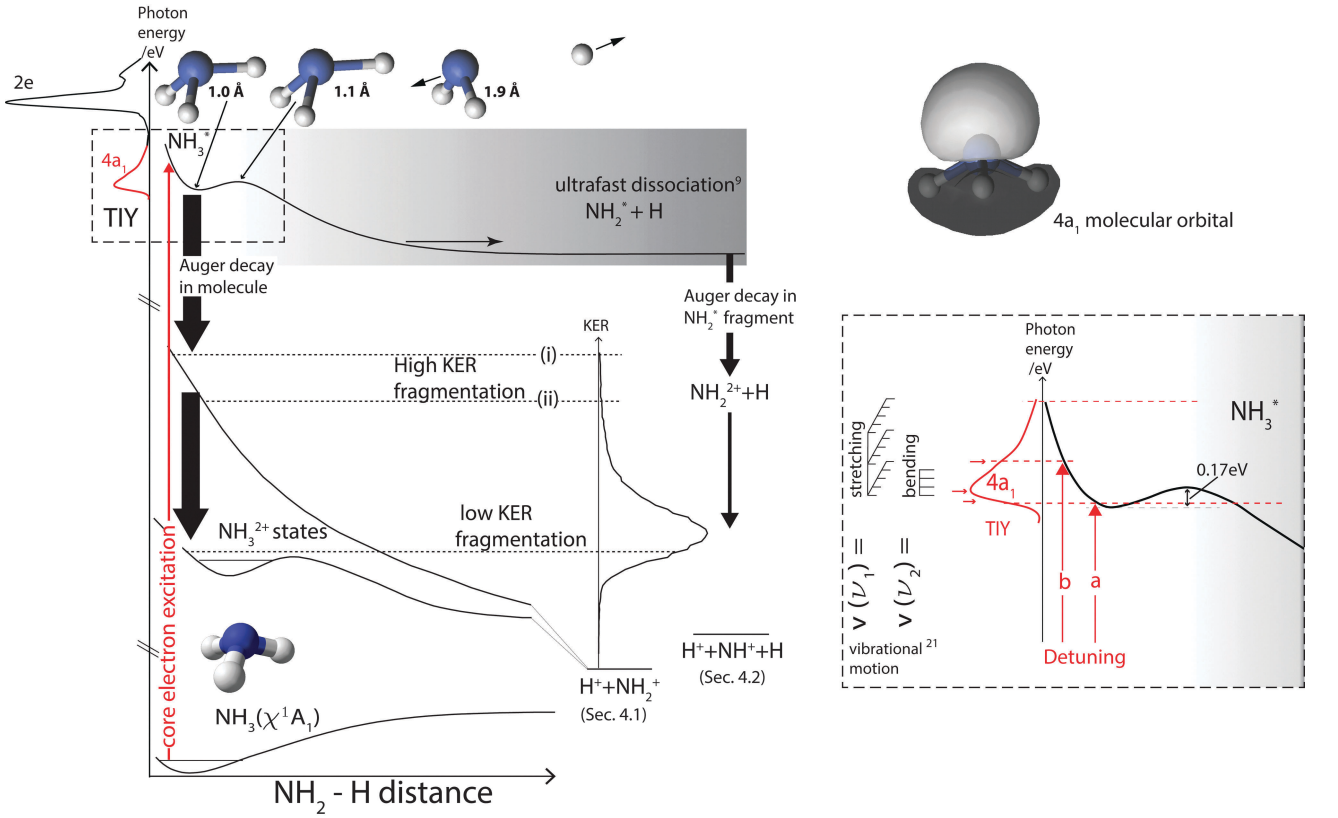

Fig. 1 Left panel: Schematic cut through the PES involved in the N1s → $4a_1$ transition. The shape of the core-excited state PES follows that indicated by our calculations. Before significant N–H bond elongation, electronic decay in the molecule produces NH_3^{2+} that can subsequently dissociate to yield $NH_2^+ + H^+$. Alternatively, if N–H bond extension is rapid, ultrafast dissociation producing a neutral H and excited NH_2* is possible. Auger decay of NH_2* and dissociation follows. Upper right panel: Illustration of the $4a_1$ molecular orbital. Lower right panel: Detuning the excitation photon energy across the $4a_1$ resonance results in excitation to different parts of the core-excited state PES. Both vibrational motion[21] and ultrafast dissociation[9] have been reported for this core-excited state.

$1a_1^2 2a_1^2 1e^4 3a_1^2$ ($\tilde{X}^1A_1$) and the LUMO (Lowest Unoccupied Molecular Orbital) is the $4a_1$ orbital. The core-excited states of NH_3 have been studied both theoretically and experimentally[29–31] and their symmetries have been confirmed by angle-resolved ion studies.[32] Both the ground state of NH_3 and the $4a_1$ core-excited state have A_1-symmetry. The $4a_1$ state is known to be of mixed Rydberg and anti-bonding valence character.[9,29]

Schematic cuts (along one N–H coordinate) through the PES of the NH_3 ground state, $\tilde{X}^1A_1$, and the $N1s^{-1}4a_1^1$ core-excited state (NH_3*) are illustrated in Fig. 1. In general relaxation of a core-excited state in a molecule proceeds *via* fluorescence or rapid Auger decay in the molecular geometry before ultrafast dissociation can occur. In the case of NH_3, Auger decay is observed to be the strongest of these two decay channels. Most of the resultant singly- or multiply-ionized final states produced *via* resonant Auger decay may undergo a further decay *via* dissociation on subpicosecond timescales. In Fig. 1 typical PES of NH_3^{2+} dication final states are illustrated along with the two fragmentation pathways that are of interest in this study – those resulting in the detected coincidences: H^+/NH_2^+ (Section 4.1) and H^+/NH^+ (Section 4.2).

When ultra-fast dissociation does occur, an excited neutral N-based fragment (NH_2*) is produced along with a neutral H fragment (Fig. 1). The NH_2* may subsequently de-excite *via* normal Auger decay to produce NH_2^{2+} which dissociates leading to the double coincidence H^+/NH^+ – which can be analysed in our data as the 3-body break-up: $H^+/NH^+/H$.

A schematic of the total ion-yield (TIY) spectrum for ammonia just below the N1s-edge (N1s I.P. 405.55(4) eV[33]) is included in Fig. 1. Detuning the photon energy across the $4a_1$ resonance results in excitation to different parts of the core-excited state PES (Fig. 1: inset).

Excitation using lower photon energies (arrow 'a') results in excitation to a bound part of the PES. In this case the molecule spends more time in the core-excited state and there is more time for nuclear motion to occur. In contrast, excitation using higher photon energies on the $4a_1$ resonance (arrow 'b') results in excitation to the repulsive (steeper) part of the PES. Due to the repulsive character of the PES in this region, faster nuclear dynamics and shorter core-excited state lifetimes are expected.

The kinetic energy released (KER) in the dissociation of the dication is dependent on that part of the dication PES to which resonant Auger decay occurred (Fig. 1). Dissociation from (i) the highest part of the PES results in a higher KER than if dissociation would occur from (ii) a lower part of the same PES to the same NH_2^+ fragment state. The kinetic energy release

distribution (KERD) recorded in our experiment corresponds to all KERs measured in the dissociation of various dication states to different N-based fragment states.

2 Experimental method

Tunable synchrotron radiation from the soft X-ray beamline I411 at the MAX IV laboratory in Lund, Sweden[34] was utilised for resonant excitation at the $N1s^{-1}4a_1^1$ state at 400.7 eV (photon energy resolution ~100 meV). At these photon energies the contribution from second-order light was negligible. The TIY spectrum recorded during these measurements (Fig. 3: lower panel) is calibrated according to the N1s → 2e peak from ref. 32 and its features agree well with previously published TIY-spectra.[29,32]

The high purity sample gas was obtained from Linde with a stated purity of 99.9999% (Ammonia 6.0). The gas sample was introduced in the interaction region of the spectrometer *via* an effusive gas jet. The background pressure in the experimental chamber was maintained at about 5×10^{-6} mbar.

For these measurements our 3D-momentum imaging Time-of-Flight (ToF) multi-coincidence spectrometer was mounted such that the ToF axis was mutually perpendicular to the direction of propagation of the synchrotron light and to the polarisation vector of the X-rays (Fig. 2). An electron detector mounted on the opposite side of the interaction region to the ToF section is used to provide the start signal for the experimental timing. The spectrometer has a two-stage acceleration with an electrostatic lens for optimal ion focussing to a delay line detector. The ROENTDEK DLD80 2-D position sensitive detector has multi-hit capability and is a high resolution timing and imaging device. We can image multiple coincidence events such as molecular fragmentation and the momenta of all ionic fragments are measured in three dimensions.[35] The complete kinematic information available to us allows us to determine the angular correlations and kinetic energy correlation between fragments for specific dissociation channels.

Data treatment involves transforming the raw experimental data recorded for each of the coincidence events into a three-dimensional momentum space.[6,26,27] Subsets of the data are then extracted by filtering by criteria for angle, momentum or fragmentation channel. For this work the direction of the polarisation vector was determined independently by measuring the angular distribution of fragments from core-excited carbon monoxide.[36]

The molecular anisotropy parameter, β, characterises the angular distribution of fragments produced in a dissociation event with respect to the polarisation vector. The conventional analytical expression for the differential photoabsorption cross section is

$$\frac{d\sigma}{d\Omega} = \frac{\sigma}{4\pi}[1 + \beta P_2(\cos\theta)], \quad (1)$$

where $d\sigma$ is the differential cross section, $d\Omega$ is the unit of solid angle, σ is the total cross section integrated over space and P_2 is the second-order Legendre polynomial, $P_2(x) = (3x^2 - 1)/2$. Fig. 2 shows the geometry of the experimental setup. The observed fragment intensity, $I(\theta)$ can be expressed as[6]

$$I(\theta) = \frac{\sigma}{2}\sin\theta[1 + \beta P_2(\cos\theta)] \quad (2)$$

and β can be estimated from a least square fit to the experimental data. For a double coincidence event, the mean of the two β-values is used. Sources of error that influence the estimated anisotropy parameter include a non-uniform detector efficiency (which would lead to an offset of the β-value), errors in the definition of the spatial and temporal center of the data and failure to properly define the direction of the polarisation vector of the incident light relative to the detector orientation. Whilst we cannot compensate for the sensitivity of β to a non-uniform detection efficiency, we can estimate its' sensitivity to the other systematic errors by translating the raw data (T, X, Y) coordinates by 3.0 ns in time and ±2.0 mm on the detector and rotating ε by 3°. For strong channels with good statistics, this led to an estimate of about ±0.05 error for β.

For a gas with randomly-oriented molecules the ensemble of resonantly-excited species will be aligned with respect to the direction of the polarisation vector of the incident (linearly-polarised) light and according to the transition symmetry. The electronic transition probability for an N1s → $4a_1$ ($A_1 \rightarrow A_1$ transition *i.e.* A_1 symmetry) excitation is at a maximum when the main symmetry axis of the molecule is oriented parallel to the polarisation vector of the absorbed radiation (Fig. 2).

In the absence of rotation[37,38] and vibronic coupling[39] the geometry of the core-excited state is projected onto ejected fragments, and can be measured in the angular distribution of ionic fragments. For rapidly-filled core-hole states the electronic decay takes place well before rotation occurs, and if dissociation is rapid then the conditions of the axial-recoil approximation are fulfilled. Under such conditions the direction of emission of ionic fragments reflects the initial molecular ion geometry. If fragmentation takes place on a subpicosecond time scale – the regime of validity of the axial-recoil approximation, then the angular anisotropy of the ejected fragment will be directly related to the angle, θ, between the molecular transition dipole moment and the broken bond (indicated in Fig. 2)[40,41]

$$\beta = 3\cos^2\theta - 1. \quad (3)$$

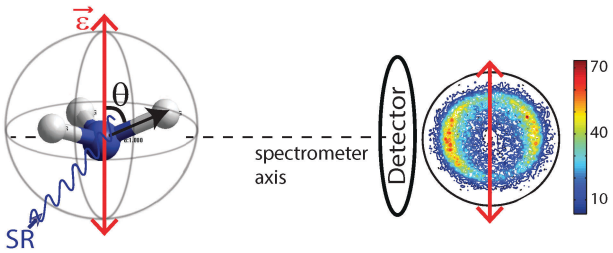

Fig. 2 Geometry of experimental setup: θ is the angle between the polarisation vector, $\vec{\varepsilon}$, and the broken molecular bond. $\vec{\varepsilon}$ is perpendicular to the propagation direction of synchrotron radiation (SR) and spectrometer axis. The expected alignment of NH_3 relative to $\vec{\varepsilon}$ for the N1s → $4a_1$ transition is indicated. Example of a detector image is included showing perpendicular ejection of H^+ fragment.

This equation is also valid for a molecule with C_{3v} symmetry undergoing a single bond break.

3 Computational details

Potential energy curves along one N–H coordinate were calculated with the MOLCAS 7 package[42] for the ground, core-excited and dication states. The extended relativistic atomic natural orbital basis sets of VTZP and VDZP quality were used for nitrogen and hydrogen, respectively. All energies were calculated using multi-configurational second-order perturbation method (CASPT2) with wavefunctions obtained from complete active space self-consistent field (CASSCF) calculations. The core hole was created by defining the occupation number of the $1a_1$ orbital to be equal to 1.00. With the $1a_1$ belonging to the restricted active space 3 (RAS3), where occupation of only one electron was allowed, we were able to maintain the core hole during the calculations.

In this work we are interested in the nuclear dynamics in the core-excited state and therefore we have followed the minimum energy path (MEP) in the core-excited state from the ground state equilibrium geometry. Here we used the SLAPAF program from the MOLCAS package with the same level of theory as described above. Energy calculations showed an existence of an energy barrier of height 0.17 eV at 1.2 Å (calculated also in ref. 9). Our calculations without any coordinate constraints predict a more open, almost planar geometry for core-excited NH_3 after vertical excitation from the ground state. We also studied the MEP for bond elongation along one N–H coordinate in the core-excited state by lengthening one N–H coordinate and allowing the other coordinates to relax. The resulting geometries are shown in the top of the Fig. 1 for N–H bond lengths 1.0 Å, 1.1 Å and 1.9 Å.

4 Results and discussion

N 1s excitation to the $4a_1$ molecular orbital has been investigated as a function of detuning the excitation photon energy across the $4a_1$ resonance:

$$NH_3 + h\nu \rightarrow NH_3^*(N1s^{-1}4a_1^1)$$

The core-excited molecule decays primarily *via* resonant Auger decay. NH_3 dications are produced in a range of electronic states that undergo further decay *via* fragmentation. The dominant fragment peaks observed in our ion ToF spectra were for H^+, N^+, NH^+ and NH_2^+. Small amounts of H_2^+ and NH_3^{2+} could also be observed. The dominant double coincidences observed in our data were: H^+/NH_2^+, H^+/NH^+ and H^+/N^+. We analyse two of these.

4.1 The H^+/NH_2^+ channel

$NH_3^{2+} \rightarrow H^+ + NH_2^+$ – single-step fragmentation to produce H^+ and NH_2^+ (in a range of vibrational, rotational and electronic states).

Dynamics and kinematics

The anisotropy parameters (β-values) for the H^+/NH_2^+ double coincidence events have been determined from the measured angular distribution of those fragments and are plotted in Fig. 3 as a function of excitation photon energy. The corresponding θ-scale (eqn (3)) is indicated on the right-hand axis of the graph. The off/below-resonance (369.8 eV) values are also included in the plot. Using trigonometry $\theta \sim 69^\circ$ for NH_3 in the ground state.

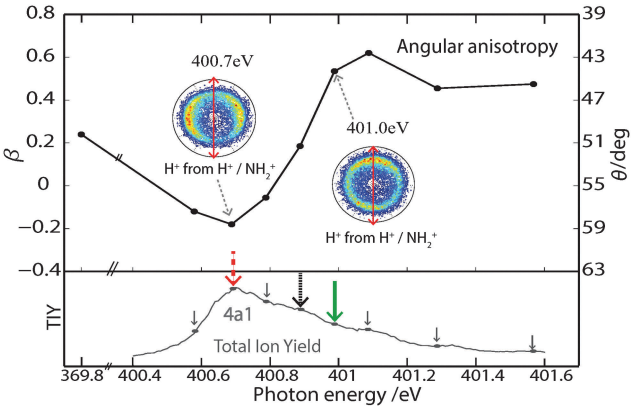

Fig. 3 Upper panel: β (anisotropy parameter) for H^+ in coincidence with NH_2^+ plotted as a function of photon energy. Right-hand axis indicates corresponding θ-scale. Lower panel: TIY across the $4a_1$ state. The coloured arrows indicate the excitation photon energies discussed in Fig. 4: 400.7 eV (red dashed), 400.9 eV (black dotted) and 401.0 eV (green).

The experimental data in Fig. 3 clearly shows an evolution of the β-value for the H^+/NH_2^+ channel as the photon energy is swept through the $4a_1$ resonance. Considering this behaviour in terms of the out-of-plane angle, θ: θ is observed to be more open following photoexcitation at low photon energies on the $4a_1$ resonance and more closed following the use of higher photon energies on the resonance. In fact detuning by just +0.3 eV from the resonance maximum corresponds to a 15° reduction in θ. This photon energy dependence could arise due to nuclear dynamics in the core-excited state or as a result of the population of different final states.

Previous measurements by Lindgren *et al.*[32] using PEPIPICO also indicated a closing of θ upon detuning to higher energies on the $4a_1$ resonance. Whereas those measurements were performed with a Wiley–McLaren type ToF mass spectrometer and the corresponding data analysis involved extensive simulations, the 3D-imaging spectrometer used to record the data presented here allows us to measure the complete kinematics of the dissociation.

Since final dication dissociation processes have characteristic kinetic energy releases (*cf.* Fig. 1), analysis of the kinetic energy release distributions (KERDs) should allow us to determine if the same/different final dissociative states and fragment states are populated as the photon energy is detuned. The KERDs recorded at 400.7 eV and 401.0 eV in Fig. 4 (upper panel) show no change in population, *i.e.* the same final dication states correlating to the $NH_2^+ + H^+$ pathway are populated. We thus conclude that, to a first approximation, the photon energy dependent geometrical distortion is not a final state effect.

We can further analyse the processes driving the observed change in β by studying the KER-filtered β-values at different photon energies (Fig. 4: lower panel). Appropriate KER filter

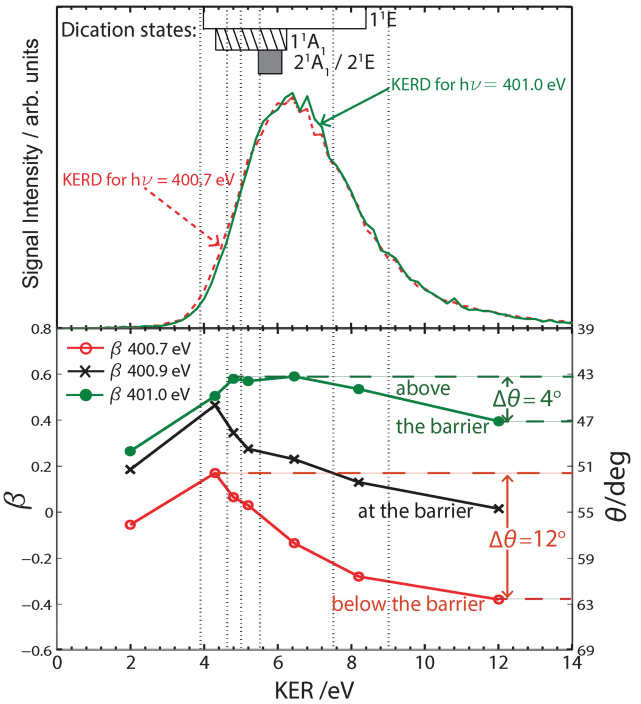

Fig. 4 Upper panel: KERDs showing the total KER in the dissociation of NH_3^{2+} to $H^+ + NH_2^+$ at $h\nu$ = 400.7 eV (red dashed) and 401.0 eV (green). KER ranges for dication states discussed in the literature are indicated at the top of the plot.[43,46,47] Lower panel: KER-filtered β-parameters for the excitation photon energies: 400.7 eV (red), 400.9 eV (black) and 401.0 eV (green) as indicated in Fig. 3. θ is observed to vary by 12° for $h\nu$ = 400.7 eV and by just 4° for $h\nu$ = 401.0 eV. Vertical dotted lines indicate the KER ranges used.

ranges (indicated by broken grey lines) were chosen based on previously reported KERs in the fragmentation of various dication final states.[43–47]

The KER-filtered β-values plotted in Fig. 4 (lower panel) as a function of KER, indicate that different geometries are associated with different dication dissociation pathways. Based on the KERs reported in the literature[43–47] as well as the KER estimates from our own work and taking fragmentation branching ratios and ToF correlation plots into account, we conclude that the dication states (dominant hole configuration): 1^1A_1 ($3a_1^{-2}$), 1^1E ($1e^{-1}3a_1^{-1}$), 2^1A_1 ($1e^{-2}$) and the 2^1E ($1e^{-2}$) contribute most to our data. These dissociation channels have previously been studied *via* inner-valence ionisation[43,44,46] and after N1s ionisation[47] but not for resonant excitation. The corresponding KERs that have been reported in the literature are indicated above the KERDs in Fig. 4 (upper panel). From these we see that the ^1E state has been associated with high KERs. In this work the ability to detune the photon energy allows us to probe the fate of excited states when they are excited to different parts of the core-excited state PES.

The KER-filtered β-values in Fig. 4 are also observed to be dependent on the excitation photon energy with those recorded following core-excitation at 400.7 eV more negative than the β s recorded following excitation at 401.0 eV, *i.e.* a larger θ is measured following excitation at the lower photon energy. If symmetric bonds are assumed the core-excited molecule would have a more open geometry at 400.7 eV.

β-values (geometries) for those states associated with KERs $>$ 4.5 eV show the strongest photon energy dependence. The data recorded at 400.7 eV shows the largest variation in β with θ varying by as much as 12°. A much narrower variation of θ is observed following photoexcitation at 401.0 eV (4°). Evidently a wider range of geometries are measured following core-excitation at the resonance maximum (400.7 eV).

Analysis of the KER-filtered β values at all photon energies on the $4a_1$ resonance (*cf.* lower panel in Fig. 3 for all photon energies measured) reveals an interesting trend. All data recorded with photon energies below 400.9 eV resulted in β curves that behave similarly to that recorded at 400.7 eV. In contrast, for photo-excitation above 400.9 eV, the resulting β curves showed similar trends to that recorded for 401.0 eV.

The geometry changes evident in the experimental data in Fig. 3 and 4 are due to a complex collection of nuclear motions in the $4a_1$ core-excited state. Geometry optimisation for this state predicts that the molecule strives for a more open, planar geometry following core-excitation. However, the extent of geometrical relaxation that is achieved depends on the time elapsed between core excitation and Auger decay. Due to the presence of a small potential energy barrier in the $4a_1$ state, core-excitation may be to a bound or unbound part of the $4a_1$ PES – the lifetime (and hence the nuclear motion that occurs) varies depending on to where on the PES excitation occurs. Core excitation at photon energies below 400.9 eV is to a bound part of the PES and the molecule can be expected to spend more time in the core excited state. Core excitation above 400.9 eV is to an unbound, dissociative part of the PES. In this case, shorter core excited state lifetimes are expected and there is less time for nuclear motion to occur. In addition, the resonant X-ray scattering duration time,[48]

$$\tau = \frac{1}{\sqrt{\Gamma^2 + \Omega^2}}, \qquad (4)$$

is at a maximum on resonance (400.7 eV in this case). This duration time is controlled by detuning the frequency of the exciting radiation from the resonance frequency and for photon energies detuned away from the resonance maximum a shorter scattering duration time is expected.[3,48,49]

Core-excitation at 400.7 eV is to a weakly bound part of the PES (arrow 'a' Fig. 1: inset). We expect a roughly 5–6 fs scattering time on resonance (Ω = 0). Due to the presence of the potential energy barrier and to the fact that the scattering duration time is at a maximum more extensive geometrical relaxation is possible (*cf.* larger θ at 400.7 eV in Fig. 3 and 4).

In contrast, for positive detuning at 401 eV (detuning by +300 meV) core-excitation is to an unbound, repulsive part of the $4a_1$ PES (arrow 'b' Fig. 1: inset). The reduced scattering time is roughly 2 fs. In this case, core-excitation above the barrier can essentially be considered to be to a dissociative state and the scattering duration time is expected to play a larger role in determining the nuclear dynamics. The shorter scattering duration time at this photon energy, allows less time for relaxation to a planar geometry. In the absence of any other nuclear motion the geometry of the molecule at the time of

Auger decay would be closer to the trigonal pyramidal arrangement, *i.e.* less open as observed in Fig. 3 for photon energies close to 400.9 eV. The reduction of θ following photoexcitation at energies above 400.9 eV in Fig. 3 can be explained as occuring due to another type of nuclear dynamics. Photoexcitation to the repulsive part of the $4a_1$ PES (*i.e.* above the potential barrier) increases the likelihood of ultrafast bond elongation.[9] MEP calculations performed as part of this analysis confirm that the molecule responds to this asymmetric bond elongation by a reduction of the H–N–H bond angles and this results in a corresponding reduction of θ. For dissociation times that are slower than the scattering duration time Auger decay may occur before dissociation can occur. However, it is possible that significant bond elongation has occurred before Auger decay, in which case we would observe this ultrafast bond elongation *via* the (resultant) closing of θ in our two-body fragmentation data. In contrast, a molecule with a faster dissociation time than the scattering duration time will undergo extensive nuclear motion leading to ultrafast dissociation before Auger decay.[13]

The more extensive variation in β observed in Fig. 4 following photoexcitation at 400.7 eV, compared to that observed at 401.0 eV can also be explained in this framework. When core excitation is to a bound part of the PES, the longer lifetime also allows for the occurrence of vibrational motion in the core-excited state and this motion is reflected in the wider range of β values (and hence θ). As aforementioned, analysis of the KER-filtered β curves for all photon energies on the $4a_1$ resonance supports this picture by clearly highlighting the distinct differences between the β-values recorded below and above 400.9 eV photon energy. The unique character of the experimental data recorded at 400.9 eV could be interpreted as arising due to core-excitation to a part of the PES that coincides with the potential barrier maximum (*i.e.* neither above nor below the barrier maximum). Our experimental data would then allow us to estimate a barrier height of about 0.2 eV which is in reasonable agreement with the value of 0.17 eV obtained from our calculations.

By continuing our analysis using a different fragmentation channel we can determine if the observed nuclear dynamics is dependent on the fragmentation channel investigated.

4.2 The $H^+/NH^+/H$ channel

$NH_3^{2+} \rightarrow H^+ + NH^+ + H$ – reaction can proceed in several steps. The fragmentation mechanisms can be illuminated with analysis.

For this analysis, the momenta of two of the fragments are measured and the momentum of the third undetected fragment (ionic or neutral) is reconstructed by using the conservation of momentum. We note that since the third fragment is undetected, we cannot determine the extent to which trication fragmentation contributes to the 3-body data presented here. However, a very low multi-coincidence signal for the pathway in question ($H^+ + H^+ + NH^+$) is observed in our data. In addition, due to the highly charged nature of the trication, we expect the dissociation of NH_3^{3+} to occur with large kinetic energy release.

Dalitz plots[50,51] are useful analytic tools for the visualisation of three-body processes where fragmentation mechanisms and the dynamics involved in dissociation can be determined. A general description for the normalised coordinates used in the Dalitz plot is:

$$\varepsilon_i = \frac{\left|\overrightarrow{p_i}\right|^2}{\sum_{i=1}^{3}\left|\overrightarrow{p_i}\right|^2}, \quad (5)$$

where $\overrightarrow{p_i}$ is the momentum vector of the fragments, $i = 1\ldots3$. A kinematic constraint $\left(\sum_i \varepsilon_i \equiv 1\right)$ dictates that all points must lie in a plane whilst conservation of linear momentum $\left(\sum_i \overrightarrow{p_i} \equiv 0\right)$ dictates that all points must lie within a circle. Use of Cartesian coordinates, $x_D = (\varepsilon_2 - \varepsilon_3)/\sqrt{3}$ and $y_D = \varepsilon_1 - 1/3$, to describe the data allows the presentation of the data in a 2D plot (Dalitz plot) which can then be used to determine the vector correlation between fragments. In the Dalitz plot the data is located within a circle of radius 1/3 inscribed in an equilateral triangle of unit height. Each Dalitz axis, i, is a vector of unit length drawn from the center of one side of the triangle ($\varepsilon_i = 0$, where particle i has zero momentum) to the opposite vertex ($\varepsilon_i = 1$). For any point in the circle the value of ε_i for the ith fragment is given by the perpendicular projection of the point onto that Dalitz axis ($\sum\varepsilon_i = 1$).

Fig. 5 contains KER-filtered Dalitz plots for the ranges indicated in the KERD in the lower half of the figure. Here we use the more specific subscripts, ε_{H^+}, ε_{NH^+} and ε_H. The data was recorded following N1s $\rightarrow$ $4a_1$ excitation at 400.7 eV. Different regions of the Dalitz plots dominate for different kinetic energy ranges. Clearly, different fragmentation mechanisms are associated with these – we can identify both sequential and concerted processes in the data.

In Fig. 5(a) the very weak signal intensity is nearly perpendicular to the ε_H axis, indicating a weak correlation between H and the other two fragments. The NH^+ and the H^+ fragments are anti-correlated to each other. Such a pattern is typical of a sequential fragmentation process in which H is ejected in the first step. In this case H is ejected with negligible momentum, whilst NH^+ and the H^+ carry away significant momentum. The features observed for 5–10 eV kinetic-energy release (Fig. 5(b)) indicate the emission of NH^+ with slightly higher momentum in a somewhat more concerted process than that observed in Fig. 5(a).

In Fig. 5(c) the feature for yet higher KER's (10–15 eV) is located symmetrically on the ε_{NH^+} axis reflecting that the two H fragments are emitted with equal momenta during a concerted breakup whilst the NH^+ fragment carries away significant kinetic energy. For the higher KER range, KER $>$ 15 eV (Fig. 5(d)), the feature is located to the right of ε_{NH^+} and implies processes with a much more concerted character than those in Fig. 5(b).

The weak feature in Fig. 5(a) could be attributed to ultrafast dissociation where loss of the H-fragment occurs before Auger decay imparting a relatively low KER to the neutral fragments. The neutral NH_2^* would subsequently undergo Auger decay to NH_2^{2+} and fragmentation into the H^+ and NH^+ ions. In this

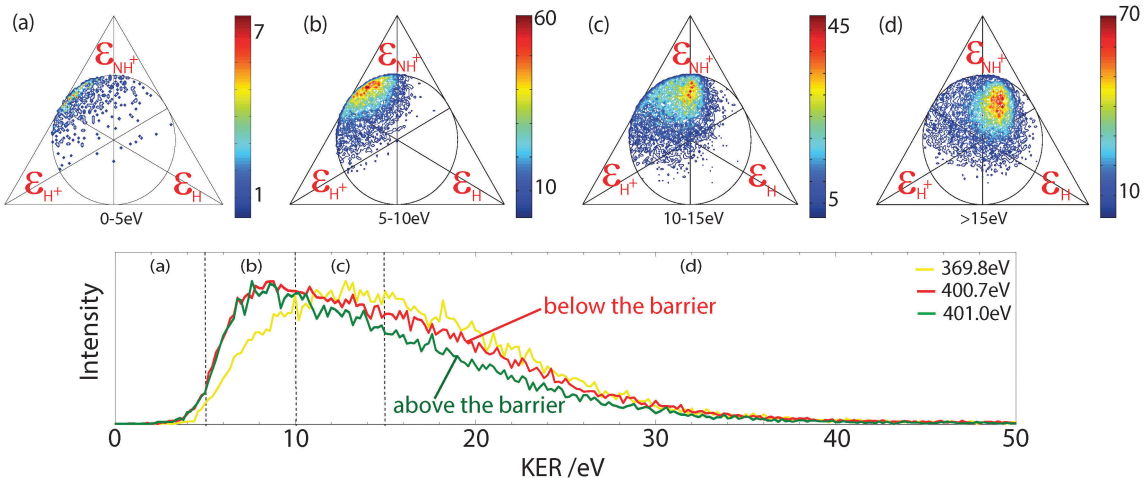

Fig. 5 Upper panel: KER-filtered Dalitz plots for the 3-body fragmentation $H^+ + NH^+ + H$ measured after photoexcitation at 400.7 eV for the KER ranges: (a) 0–5 eV, (b) 5–10 eV, (c) 10–15 eV and (d) >15 eV. Lower panel: Kinetic energy release distributions after photoexcitation at 369.8 eV, 400.7 eV and 401.0 eV.

second step, the Coulomb repulsion would result in higher fragment kinetic energies.

The signal intensity in Fig. 5(b) for the 5–10 eV KER range and in Fig. 5(d) for KER > 15 eV, are the result of asynchronous dissociation mechanisms. The data in Fig. 5(b) could arise due to asymmetric bond elongation directly before fragmentation. Asynchronous concerted processes, for example, non-pure sequential fragmentation (in which the second step is not completely independent of the first step[52]) are likely causes for the signal observed in Fig. 5(d). Note that since two of the three fragments are actually measured, the undetected particle may be either H or H^+.

In the 10–15 eV KER interval (Fig. 5(c)) the symmetric ejection of hydrogen fragments takes place in the dissociation of the trication. An event producing the three ionic fragments, $H^+ + H^+ + NH^+$, may be detected as a double coincidence since the probability of detecting two H^+ from the same dissociation is affected by the finite detection efficiency of the detector and the electronics dead time (~20 ns) such that the resulting multi-ion detection deadtime ranges between 20–100 ns (depending on the temporal separation of the ion hits and their corresponding $[x,y]$-positions on the DLD detector).

The evolution of the Dalitz plots as a function of photon energy is investigated in Fig. 6 for the photon energies (a) 369.8 eV, (b) 400.7 eV and (c) 401.0 eV. In these diagrams no KER filtering has been performed. The corresponding KERDs are plotted in the lower column of Fig. 5. Two distinct features (denoted '1' and '2') are apparent in the Dalitz plots. Comparison with the KER-filtered Dalitz plots in Fig. 5 reveals that feature '1' which dominates for photoexcitation at 369.8 eV is related to high KER processes. This is also evident in the KERD for 369.8 eV in the lower half of Fig. 5. Feature '2' is present following photoexcitation at 400.7 eV and is associated with low kinetic energy release. At 401.0 eV feature '2' is observed to dominate in the Dalitz plot. Again, these trends are clearly observable in the KERDs of Fig. 5.

As the excitation photon energy is detuned across the $4a_1$ resonance, we excite to different parts of the core-excited state

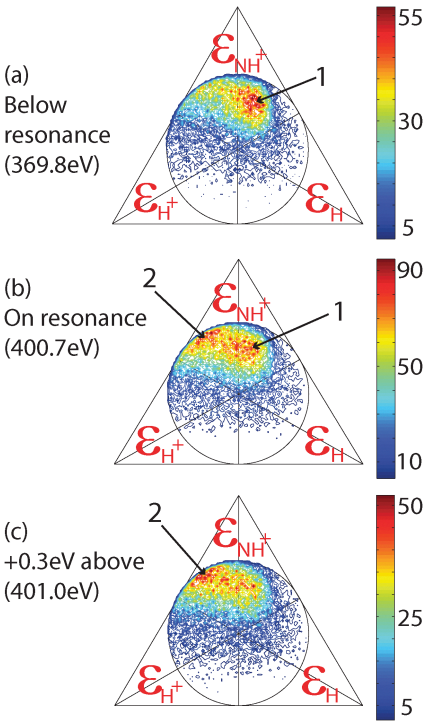

Fig. 6 Dalitz plots for the 3-body fragmentation $H^+ + NH^+ + H$ measured after photoexcitation at (a) 369.8 eV (b) 400.7 eV (c) 401.0 eV.

PES and different types of nuclear motion influence the experimental data that we observe. It is clear that a number of different fragmentation processes contribute to the three-body data presented here. The Low KER processes become increasingly dominant as the excitation photon energy is increased (*cf.* KERDs in Fig. 5: lower panel and Dalitz plots in Fig. 6). Photoexcitation at 401 eV results in excitation to the unbound, steep part of the $4a_1$ PES (arrow 'b' in Fig. 1: inset). In this case ultrafast bond elongation and even ultrafast dissociation is possible. The signature

features observed in the KER-filtered Dalitz plots in Fig. 5(a) and (b) provide evidence for both ultrafast bond elongation and dissociation. The increase in intensity of these features when the excitation photon energy is detuned to higher values (compare Fig. 6(b) and (c)) also provides firm evidence for the occurrence of ultra-fast dissociation in this fragmentation channel. Clearly the three-body data strongly supports the extensive picture proposed in Section 4.1 in which ultrafast bond elongation was interpreted to occur at higher excitation photon energies. In the case where bond elongation occurs before Auger decay, a different part of the dication (or trication) PES will be reached at somewhat longer internuclear N–H distances than if Auger decay occurs from the bound part of the $4a_1$ PES. This will also influence the measured KERs.

5 Conclusions

The nuclear dynamics induced following core-electron excitation to the $N1s^{-1}4a_1^1$ state of the ammonia molecule have been investigated. The kinematics of the two-body fragmentation channel, H^+/NH_2^+ and the 3-body fragmentation channel, $H^+/NH^+/H$ have been analysed. In both cases our experimental data provides evidence of complex nuclear motion in the core-excited state.

In the case of the H^+/NH_2^+ 2-body fragmentation channel we report indirect observation of geometrical distortion of the molecule *via* the evolution of the fragment ion anisotropy as the core-excited state PES is probed by detuning the excitation photon energy across the $N1s^{-1} \rightarrow 4a_1$ resonance. Three types of nuclear motion contribute to the photon energy dependent angular anisotropy observed for this pathway.

Based on our analysis we assert that detuning the photon energy results in excitation to different parts of the core-excited state PES. Excitation to a bound part of the $N1s^{-1}4a_1^1$ PES means that the molecule spends a longer time in the core-excited state before Auger decay occurs. The dominant nuclear motion that is initiated as a result of this core excitation involves a relaxation of the molecule towards a more planar geometry. The extent of relaxation achieved by the molecule depends on the time delay before Auger decay. In addition, vibrational motion also has time to occur and we see some experimental evidence to suggest the occurrence of such a motion in our data. Indeed, vibrational motion has previously been discussed for this core-excited state of ammonia.[21]

In contrast, core-excitation using photon energies >400.9 eV results in excitation to a steep unbound part of the PES. The scattering duration time is also significantly reduced at these detuned photon energies. The molecule has less time to undergo geometrical relaxation to a planar geometry and hence remains in a more pyramidal arrangement. No vibrational motion is possible. However, depending on the scattering duration time and the dissociation time of the molecule, ultrafast bond elongation may occur before Auger decay.[9] Our calculations indicate that the molecule will respond to such an asymmetric bond elongation by reduction of its bond angles and this is observed in our H^+/NH_2^+ data as a closing of the out-of-plane angle, θ.

The 3-body fragmentation channel contains evidence for the enhancement of an asynchronous bond extension as well as a weak signal from ultrafast dissociation following core electron excitation on and above the resonance maximum. The observation of such nuclear motion at higher photon energies is in agreement with the observation of a bond elongation at higher excitation photon energies in the two-body data and strongly supports the conclusions made in Section 4.1.

Acknowledgements

We gratefully acknowledge assistance from the MAX IV Laboratory staff, in particular Maxim Tchaplyguine. Funding for this work was granted by the Swedish Research Council (VR). A. Sankari would also like to acknowledge financial support from the Academy of Finland.

References

1 R. Feifel and M. N. Piancastelli, *J. Electron Spectrosc. Relat. Phenom.*, 2011, **183**, 10.
2 *Handbook of High-resolution Spectroscopy*, ed. M. Quack and F. Merkt, Wiley Publishing, Florida, 2011, pp. 1655–1690.
3 O. Björneholm, S. Sundin, S. Svensson, R. R. T. Marinho, A. Naves de Brito, F. Kh. Gel'mukhanov and H. Ågren, *Phys. Rev. Lett.*, 1997, **79**, 3150.
4 D. Céolin, C. Miron, M. Simon and P. Morin, *J. Electron Spectrosc. Relat. Phenom.*, 2004, **141**, 171.
5 K. Ueda and J. H. D. Eland, *J. Phys. B: At., Mol. Opt. Phys.*, 2005, **38**, S839.
6 J. Laksman, D. Céolin, M. Gisselbrecht, S. E. Canton and S. L. Sorensen, *J. Chem. Phys.*, 2009, **131**, 244305.
7 U. Ekström, V. Carravetta, M. Alagia, M. Lavollee, R. Richter, C. Bolcato and S. Stranges, *J. Chem. Phys.*, 2008, **128**, 044302.
8 M. Simon, C. Miron, N. Leclercq, P. Morin, K. Ueda, Y. Sato, S. Tanaka and Y. Kayanuma, *Phys. Rev. Lett.*, 1997, **79**, 3857.
9 I. Hjelte, M. N. Piancastelli, C. M. Jansson, K. Wiesner, O. Björneholm, M. Bässler, S. L. Sorensen and S. Svensson, *Chem. Phys. Lett.*, 2003, **370**, 781.
10 J. Laksman, E. P. Månsson, A. Sankari, D. Céolin, M. Gisselbrecht and S. L. Sorensen, *Phys. Chem. Chem. Phys.*, 2013, **15**, 19322.
11 K. Ueda, A. de Fanis, N. Saito, M. Machida, K. Kubozuka, H. Chiba, Y. Muramatu, Y. Sato, A. Czasch, O. Jaguzki, R. Dörner, A. Cassimi, M. Kitajima, T. Furuta, H. Tanaka, S. L. Sorensen, K. Okada, S. Tanimoto, K. Ikejiri, Y. Tamenori, H. Ohashi and I. Koyano, *Chem. Phys.*, 2003, **289**, 135.
12 P. Morin and C. Miron, *J. Electron Spectrosc. Relat. Phenom.*, 2012, **185**, 259.
13 P. Morin and I. Nenner, *Phys. Rev. Lett.*, 1986, **56**, 1913.
14 H. Aksela, S. Aksela, M. Ala-Korpela, O.-P. Sairanen, M. Hotokka, G. M. Bancroft, K. H. Tan and J. Tulkki, *Phys. Rev. A: At., Mol., Opt. Phys.*, 1990, **41**, 6000.

15 A. Menzel, B. Langer, J. Viefhaus, S. B. Whitfield and U. Becker, *Chem. Phys. Lett.*, 1996, **258**, 265.
16 S. J. Schaphorst, C. D. Caldwell, M. O. Krause and J. Jimenez-Mier, *Chem. Phys. Lett.*, 1993, **213**, 315.
17 C. D. Caldwell, S. J. Schaphorst, M. O. Krause and J. Jimenez-Mier, *J. Electron Spectrosc. Relat. Phenom.*, 1994, **67**, 243.
18 A. Naves de Brito, Al. Naves de Brito, O. Björneholm, J. S. Neto, A. B. Machado, S. Svensson, A. Ausmees, S. J. Osborne, L. J. Sæthre, H. Aksela, O.-P. Sairanen, A. Kivimäki, E. Nõmmiste and S. Aksela, *THEOCHEM*, 1997, **394**, 135.
19 P. Sałek, V. Carravetta, F. Kh. Gel'mukhanov, H. Ågren, B. Schimmelpfennig, M. N. Piancastelli, S. L. Sorensen, R. Feifel, I. Hjelte, M. Bässler, S. Svensson, O. Björneholm and A. Naves de Brito, *Chem. Phys. Lett.*, 2001, **343**, 332.
20 I. Hjelte, M. N. Piancastelli, R. F. Fink, O. Björneholm, M. Bässler, R. Feifel, A. Giertz, H. Wang, K. Wiesner, A. Ausmees, C. Miron, S. L. Sorensen and S. Svensson, *Chem. Phys. Lett.*, 2001, **334**, 151.
21 Y. Senba, T. Goya, H. Yoshida and A. Hiraya, *J. Electron Spectrosc. Relat. Phenom.*, 2005, **144**, 195.
22 J. H. D. Eland, F. S. Wort and R. N. Royds, *J. Electron Spectrosc. Relat. Phenom.*, 1986, **41**, 297.
23 J. H. D. Eland and A. H. Pearson, *Meas. Sci. Technol.*, 1990, **1**, 36.
24 K. Ueda, E. Shigemasa, Y. Sato, A. Yagishita, T. Sasaki and T. Hayaishi, *Rev. Sci. Instrum.*, 1989, **60**, 2193.
25 J. H. D. Eland, M. Tashiro, P. Linusson, M. Ehara, K. Ueda and R. Feifel, *Phys. Rev. Lett.*, 2010, **105**, 213005.
26 J. Laksman, D. Céolin, M. Gisselbrecht and S. L. Sorensen, *J. Chem. Phys.*, 2010, **133**, 144314.
27 J. Laksman, E. P. Månsson, C. Grunewald, A. Sankari, M. Gisselbrecht, D. Céolin and S. L. Sorensen, *J. Chem. Phys.*, 2012, **136**, 104303.
28 G. Herzberg, *Molecular Spectra and Molecular Structure*, Krieger Publishing, Florida, 1966, vol. III, p. 609.
29 J. Schirmer, A. B. Trofimov, K. J. Randall, J. Feldhaus, A. M. Bradshaw, Y. Ma, C. T. Chen and F. Sette, *Phys. Rev. A: At., Mol., Opt. Phys.*, 1993, **47**, 1136.
30 A.-F. Niu, Y. Zhang, W.-H. Zhang and J.-M. Li, *Phys. Rev. A: At., Mol., Opt. Phys.*, 1998, **57**, 1912.
31 A. Jürgensen and R. G. Cavell, *Chem. Phys.*, 2001, **273**, 77.
32 A. Lindgren, M. Gisselbrecht, F. Burmeister, A. Naves de Brito, A. Kivimäki and S. L. Sorensen, *J. Chem. Phys.*, 2005, **122**, 114306.
33 R. W. Shaw, J. S. Jen and T. D. Thomas, *J. Electron Spectrosc. Relat. Phenom.*, 1977, **11**, 91.
34 M. Bässler, A. Ausmees, M. Jurvansuu, R. Feifel, J.-O. Forsell, P. de TarsoFonseca, A. Kivimäki, S. Sundin, S. L. Sorensen, R. Nyholm, O. Björneholm, S. Aksela and S. Svensson, *Nucl. Instrum. Methods Phys. Res., Sect. A*, 2001, **469**, 382.
35 J. Laksman, D. Céolin, E. P. Månsson, S. L. Sorensen and M. Gisselbrecht, *Rev. Sci. Instrum.*, 2013, **84**, 123113.
36 L. Journel, R. Guillemin, A. Haouas, P. Lablanquie, F. Penent, J. Palaudoux, L. Andric, M. Simon, D. Céolin, T. Kaneyasu, J. Viefhaus, M. Braune, W. B. Li, C. Elkharrat, F. Catoire, J.-C. Houver and D. Dowek, *Phys. Rev. A: At., Mol., Opt. Phys.*, 2008, **77**, 042710.
37 R. N. Zare, *Mol. Photochem.*, 1972, **4**, 1.
38 R. M. Wood, Q. Zheng, A. K. Edwards and M. A. Mangan, *Rev. Sci. Instrum.*, 1997, **68**, 1382.
39 N. Kosugi, *J. Electron Spectrosc. Relat. Phenom.*, 1996, **79**, 351.
40 J. D. Bozek, N. Saito and I. H. Suzuki, *Phys. Rev. A: At., Mol., Opt. Phys.*, 1995, **51**, 4563.
41 T. Gejo, Y. Takata, T. Hatsui, M. Nagasono, H. Oji, N. Kosugi and E. Shigemasa, *Chem. Phys.*, 2003, **289**, 15.
42 F. Aquilante, L. de Vico, N. Ferré, G. Ghigo, P.-Å. Malmqvist, P. Neogrády, T. B. Pedersen, M. Pitoňák, M. Reiher, B. O. Roos, L. Serrano-Andrés, M. Urban, V. Veryazov and R. Lindh, *J. Comput. Chem.*, 2010, **31**, 224.
43 D. Winkoun and G. Dujardin, *Z. Phys. D: At., Mol. Clusters*, 1986, **4**, 57.
44 R. K. Boyd, S. Singh and J. H. Beynon, *Chem. Phys.*, 1985, **100**, 297.
45 J. H. D. Eland, F. S. Wort, P. Lablanquie and I. Nenner, *Z. Phys. D: At., Mol. Clusters*, 1986, **4**, 31.
46 M. Stankiewicz, P. A. Hatherly, L. J. Frasinski, K. Codling and D. M. P. Holland, *J. Phys. B: At., Mol. Opt. Phys.*, 1989, **22**, 21.
47 C. I. Ma, D. M. Hanson, K. Lee and R. G. Hayes, *J. Electron Spectrosc. Relat. Phenom.*, 1995, **75**, 83.
48 A. Baev, P. Sałek, F. Kh. Gel'mukhanov, H. Ågren, A. Naves de Brito, O. Björneholm and S. Svensson, *Chem. Phys.*, 2003, **289**, 51.
49 M. N. Piancastelli, G. Goldsztejn, T. Marchenkol, R. Guillemin, R. K. Kushawaha, L. Journel, S. Carniato, J.-P. Rueff, D. Céolin and M. Simon, *J. Phys. B: At., Mol. Opt. Phys.*, 2014, **47**, 124031.
50 R. H. Dalitz, *Philos. Mag.*, 1953, **44**, 1068.
51 N. Neumann, D. Hant, L. Ph. H. Schmidt, J. Titze, T. Jahnke, A. Czasch, M. S. Schöffler, K. Kreidi, O. Jagutzki, H. Schmidt-Böcking and R. Dörner, *Phys. Rev. Lett.*, 2010, **104**, 103201.
52 N. Neumann, A. Czasch, D. Hant, O. Jagutzki, T. Jahnke, H.-K. Kim, K. Kreidi, L. Ph. H. Schmidt, M. S. Schöffler, J. Titze, B. Ullrich, R. Wallauer, H. Schmidt-Böcking and R. Dörner, *J. Phys.: Conf. Ser.*, 2009, **194**, 102025.